Quantum confinement effects in doped two-dimensional Si layers: Novel device design for two-dimensional pn-junction structures

2014 Jpn. J. Appl. Phys. 53 04EC08

(http://iopscience.iop.org/1347-4065/53/4S/04EC08)

Japanese Journal of Applied Physics **53**, 04EC08 (2014) **REGULAR PAPER**
http://dx.doi.org/10.7567/JJAP.53.04EC08

Quantum confinement effects in doped two-dimensional Si layers: Novel device design for two-dimensional pn-junction structures

Tomohisa Mizuno[1]*, Yuhta Nakahara[1], Yuhsuke Nagata[1], Yuhya Suzuki[1], Takashi Aoki[1], and Toshiyuki Sameshima[2]

[1]*Department of Science, Kanagawa University, Hiratsuka, Kanagawa 259-1293, Japan*
[2]*Department of Engineering, Tokyo University of Agriculture and Technology, Koganei, Tokyo 184-8588, Japan*
E-mail: mizuno@info.kanagawa-u.ac.jp

Received September 14, 2013; revised October 23, 2013; accepted November 17, 2013; published online February 13, 2014

We have experimentally studied the impurity dopant atom effects on band structure modulation (BSM) and phonon confinement effects (PCEs) in a two-dimensional (2D) Si layer. By the photoluminescence (PL) method, the effect of the dopant atom on the bandgap (E_G) of 2D-Si is found to be very small. However, the E_G narrowing effects of n^+ 2D-Si are much smaller than those of conventional 3D n^+-Si, which is characteristic of 2D-Si. On the other hand, Raman spectroscopy shows that the PCEs are completely independent of the phosphorous dopant density of n^+ 2D-Si. Using the experimental BSM of 2D-Si, we introduce a device design for pn junction structures in 2D-Si for future complementary metal oxide semiconductor (CMOS) devices, to suppress the built-in potential increase of the pn junction, in spite of the E_G expansion in the 2D-Si channel region.

1. Introduction

Two-dimensional (2D) Si structures are widely used for extremely thin silicon-on-insulator (ETSOI) field-effect transistors (FETs) and 3D metal–oxide–semiconductor (MOS) devices, such as FinFETs,[1,2] as well as Si photonic devices.[3,4] In addition, surface orientation engineering[5] and a strain technique[6] have been the major technologies for realizing high-performance complementary MOS (CMOS) devices. To improve the short-channel effects (SCEs) of MOSFETs and the photoluminescence (PL) intensity of Si photonic devices, the 2D Si thickness T_S should continuously be scaled down.[1,2–4] However, the quantum confinement effects (QCEs) in a thinner T_S structure cause electron mobility modulation,[7–9] which is due to the QCEs of 2D electrons in ETSOIs. In addition, the QCEs induce band structure modulation (BSM), resulting in the band gap E_G expansion of ETSOIs.[10–12]

On the other hand, the first-order Raman scattering phonon energy is the longitudinal optical phonon (LO) energy ($E_{P0} \sim 64$ meV) at $\boldsymbol{q} \approx 0$ (Γ point in the Brillouin zone), where $\boldsymbol{q}$ is the wave vector of the scattered phonons.[13,14] However, in a low-D Si structure, the finite Si size effects result in the quantum phonon uncertainty Δq due to Heisenberg's uncertainty principle; thus, Δq relaxes the momentum conservation and first-order Raman selection rule[14] in the phonon dispersion curve, which is attributable to the participation of phonons away from the Γ point.[15–21] As a result, Raman peaks with a wave number less than 520 cm^{-1} at the Γ point also become active in low-D Si; thus, the phonon confinement effects (PCEs) cause a downshift and an asymmetric broadening of Raman peaks.[15–18,21] PCEs are reported to be enhanced in 1D and 0D Si semiconductors, such as Si nanowires (1D)[16,21] and nanocrystals (0D),[16,20] compared with those in ETSOIs, because Δq increases with decreasing Si dimensions from 2D to 0D. In the case of 2D Si, the finite Si thickness T_S results in the phonon wave vector uncertainty Δq_L in the longitudinal direction of 2D-Si, that is, $\Delta q_L \approx 1/T_S$. As a result, PCEs also occur even in 2D Si. Therefore, PCEs induce carrier mobility reduction owing to the enhanced phonon scattering of carriers even in ETSOIs.[22] Moreover, the drain current drivability of 2D Si devices is also degraded by self-heating effects in ETSOI structures, because of the large heat resistance of the buried oxide layer (BOX) in ETSOIs.[1] Therefore, it is very important to study the 2D phonon properties as well as the modulated band structures of the 2D Si layer, to clarify both the phonon-induced carrier velocity reduction and thermal properties (such as thermal conductivity) of 2D Si structures. Recently, we experimentally demonstrated the asymmetrical broadening and peak downshift of Raman intensities owing to PCEs even in (100) and (110) 2D Si with $T_S \approx a$ fabricated by the thermal oxidation of SOIs,[23,24] where a is the Si lattice constant of 0.543 nm. As a result, PCEs are independent of the surface orientation and the tensile strain of 2D-Si.[24]

QCEs modulate the energy-band structures of 2D Si and change the Si crystals to a direct-bandgap material from an indirect-bandgap 3D Si.[4,10,22,25] As a result, even in the Si material, PL has been observed in low-dimensional porous-Si (p-Si),[26] polycrystalline Si,[27] and even thin-film Si,[4,22,28,29] as a result of BSM. In particular, it is also reported that the T_S dependence of the PL peak photon energy E_{PH} is caused by the direct optical transmission in the direct-bandgap thin-film Si material that is changed from an indirect-bandgap bulk Si material.[25] Actually, by the PL method, we demonstrated the T_S dependence of E_{PH} in (100) 2D-Si.[24] However, we could not detect the PL intensity from (110) 2D-Si, which is probably because (110) 2D-Si still has an indirect-bandgap structure.[24] In addition, the PL properties of (100) 2D-Si strongly depend on the excitation photon energy.[24]

pn junctions are also of great importance for realizing future CMOS devices. However, the QCEs even in a doped 2D-Si layer have not yet been studied in detail. Therefore, it is impossible to reconstruct the device design for pn junctions in MOSFETs composed of 2D-Si layers. Thus, it is very important to study the impurity dopant density dependence of the BSM and the PCEs in 2D-Si layers.

In this work, we experimentally studied the dopant atom effects on the BSM and PCEs in n^+ and p^- 2D-Si layers fabricated by the oxidation-induced thinning of SOIs after impurity ion implantation.[30] By PL and Raman analyses, we clarified both the BSM and PCEs differences between the doped 2D-Si and 2D intrinsic Si layers (2D i-Si). Next, we discussed the optimum pn-junction structures in the 2D-Si, considering the BSM in the doped and non-doped 2D-Si layers. Finally, we showed the technical limitation for

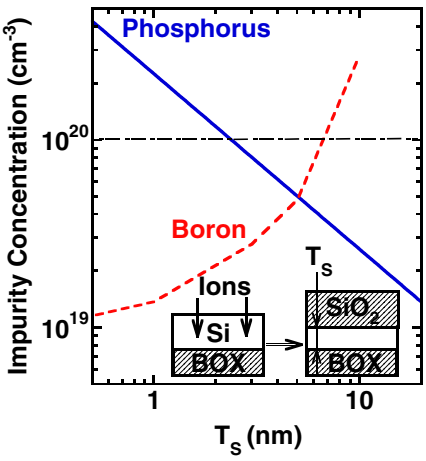

Fig. 1. (Color online) Simulated impurity densities of phosphorus (solid line) and boron (dashed line) of 2D-Si layers thinned by oxidation technique after impurity ion implantation as a function of T_S. The inset shows the fabrication process for 2D-Si layers by oxidizing SOI (right panel) after impurity ion implantation into initial SOIs (left panel). The P^+ and B^+ segregation coefficients at the Si/SiO_2 interface, during the oxidation of SOI substrates, are about 10 ($\gg 1$) and 0.1 ($\ll 1$), respectively.[32] As a result, the P^+ density in the 2D-Si layers increases, but the B^+ density rapidly decreases.

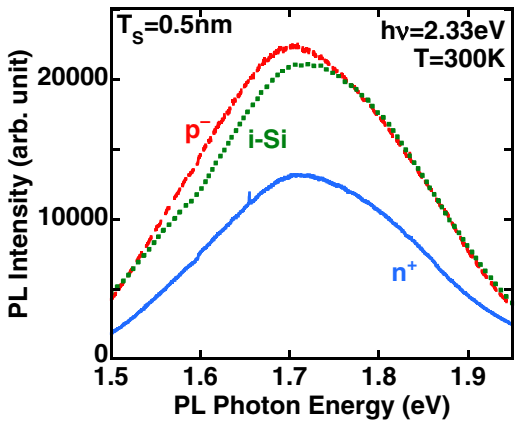

Fig. 2. (Color online) PL spectra of n^+ (solid line), p^- (dashed line), and i-Si (dotted line) layers, where $T_S \approx 0.5$ nm, $T = 300$ K, and $h\nu = 2.33$ eV. Photon energy at peak I_{PL} for doped 2D-Si is slightly lower than that of i-Si. The PL intensity of the n^+ layer is reduced.

fabricating heavily doped 2D-Si, by showing Si dot formation during the fabrication of 2D-Si.

2. Experimental procedure

To study the pn junction of 2D-Si, the target impurity concentrations of the source/drain n^+ and the channel p^- in 2D-Si layers are higher than 1×10^{20} and about 1×10^{19} cm^{-3}, respectively, in this study. This p^- density is the upper limit of the channel dopant for inhibiting the tunnel current at the pn junction. The inset in Fig. 1 shows the process steps for fabricating doped 2D-Si. The n^+ and p^- 2D-Si layers were fabricated by thermal-oxidation-induced thinning of surface Si layers on a BOX layer at 1000 °C after phosphorus P^+ and boron B^+ ion implantation into bonded (100) SOI substrates,[31] respectively. The P^+ and B^+ segregation coefficients m_P and m_B at the Si/SiO_2 interface, during the oxidation of the SOI substrates, are about 10 and 0.1, respectively.[32] As a result, after the oxidation of the SOIs, it is expected that the P^+ density (N_D) of the 2D-Si layers increases, but that the B^+ density (N_A) rapidly decreases.[32] Thus, in this study, the P^+ and B^+ ion doses are determined by the process simulator,[33] shown as the simulated N_D and N_A as a function of T_S after thinning the SOIs with T_S in Fig. 1, where the P^+ and B^+ doses were 4×10^{13} cm^{-2} for initial 56-nm-thick SOIs and 3×10^{15} cm^{-2} for the initial 10-nm-thick SOIs, respectively. With the thinning of the SOIs, N_D continuously increases, but N_A continuously decreases, as expected. As a result, at $T_S \leq 2$ nm, N_D is higher than 1×10^{20} cm^{-3} and N_A becomes about 1×10^{19} cm^{-3}, which are the target concentrations in this study.

In addition, relatively low-n^+ 2D-Si layers were also fabricated using a P^+ dose of 1×10^{13} cm^{-2}. On the other hand, very high n^+ 2D-Si layers, shown in Sect. 3.4, were formed using a P^+ dose of 1×10^{15} cm^{-2}.

The T_S of the 2D-Si layers was evaluated by the UV/visual reflection spectrum method[23] and was also confirmed by high-resolution transmission electron microscopy (HRTEM). At room temperature, we analyzed both the E_G properties evaluated by the PL method with a 2.33 eV (532 nm) excitation laser and the PCEs results obtained by UV (325 nm) Raman spectroscopy for doped Si, compared with those for i-Si. The laser power P_L was set to be 1 mW to compress the P_L-induced heating effects of 2D-Si,[24] and the laser diameter was 1 μm.

The N_D and N_A values of 2D-Si layers are estimated using the process simulator shown in Fig. 1. In addition, the dopant impurity density in a very heavily doped Si dot shown in Sect. 3.4 is obtained by energy dispersion X-ray (EDX) analysis.

3. Results and discussion

3.1 Energy-band structure modulation of doped 2D-Si

(100) 2D-Si has a direct-bandgap structure,[3] and thus its peak PL energy E_{PH} is considered to be equal to the E_G of 2D-Si.[24]

Figure 2 shows the PL spectra of 2D n^+, p^-, and i-Si layers at $T_S \approx 0.5$ nm. All the n^+, p^-, and intrinsic 2D-Si structures have almost the same PL spectra and their E_{PH} values in all 2D-Si are approximately 1.7 eV. However, the E_{PH} of the doped 2D-Si is slightly lower than that of i-Si. In addition, the PL intensity I_{PL} of the n^+ 2D-Si is reduced, which may be attributable to the reduction in the PL emission efficiency of the heavily doped 2D-Si. The I_{PL} reduction of the heavily doped 2D-Si is similar to the results that I_{PL} in heavily doped Si-nanocrystals decreases with increasing impurity dopant density.[34]

Figure 3 shows the E_{PH} mapping data of n^+ 2D-Si in a 100 μm^2 area. The E_{PH} distribution is almost uniform. Namely, the E_{PH} variation is very small, and the standard deviation in E_{PH}, δE_{PH}, is only 0.01 eV, which is almost the same as those in both 2D p^- and i-Si layers. Since E_{PH} strongly depends on T_S,[24] the small δE_{PH} indicates that the T_S deviation is also very small.

Here, the relationship between E_{PH} and T_S is shown in Fig. 4, where the T_S deviation δT_S was estimated to be about 0.2 nm in our previous study,[24] and the error bar of E_{PH} shows a δE_{PH} of 0.01 eV. The E_{PH} values of the 2D n^+ and

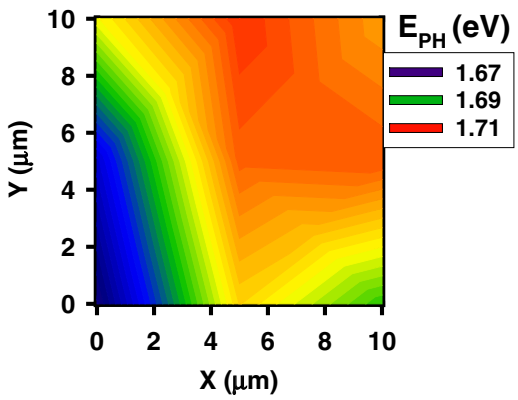

Fig. 3. (Color online) PL peak photon energy E_{PH} mapping of n^+ 2D-Si layers, where $T_S \approx 0.5$ nm, $T = 300$ K, and $h\nu = 2.33$ eV. E_{PH} variation is very small in a 100 μm^2 area and the standard deviation is only about 0.01 eV.

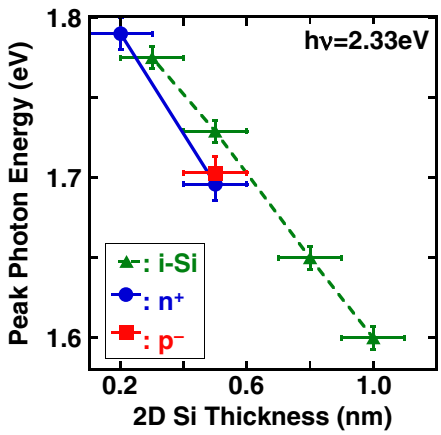

Fig. 4. (Color online) T_S dependence of E_{PH} at $T = 300$ K. Circles, squares, and triangles show the experimental results for n^+, p^-, and i-Si layers, respectively. The error bar of E_{PH} is 0.01 eV obtained from Fig. 3, and the error bar of T_S was about 0.2 nm.[24] E_{PH} of doped 2D-Si also increases with decreasing T_S, but is slightly lower than that of 2D i-Si. Here, data for i-Si can be fitted by $E_{PH} = 1.85 - 0.25T_S$, where the correlation coefficient is 0.999.

i-Si layers rapidly increase with decreasing T_S, and the E_{PH} of the 2D i-Si layers can be experimentally fitted using the following formula.[13]

$$E_{PH}\ (\mathrm{eV}) = 1.85 - 0.25T_S\ (\mathrm{nm}). \tag{1}$$

In addition, the E_{PH} of doped 2D-Si is slightly smaller than that of i-Si. This result is probably due to the bandgap narrowing δE_G effects in heavily doped Si, which is attributable to the stored electrostatic energy of majority–minority carrier pairs in the case of 3D-Si.[13]

Here, δE_G is defined as $\delta E_G \equiv E_{PHI} - E_{PHD}$, where E_{PHI} and E_{PHD} are the E_{PH} values of i-Si and doped Si, respectively. Figure 5 shows δE_G as a function of an impurity dopant density obtained by the process simulator.[33] The solid line shows the calculated δE_G of 3D-Si, which is empirically given by the following equation:

$$\delta E_G\ (\mathrm{meV}) = 18.7 \ln(N/7 \times 10^{17}), \tag{2}$$

where N is the dopant density (cm^{-3}).[13]

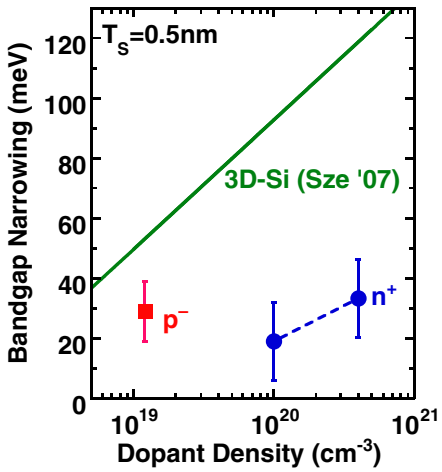

Fig. 5. (Color online) Bandgap narrowing of doped 2D-Si vs dopant density, where $T_S \approx 0.5$ nm. Circles and square show the data of n^+ and p^- 2D-Si, respectively. The solid line shows the calculated δE_G values of 3D-Si calculated using Eq. (2).[13] E_G narrowing of doped 2D-Si is almost independent of the dopant density and is much lower than that of doped 3D-Si.

The δE_G of doped 2D-Si is only about 30 meV and is almost independent of N in this study, although the δE_G of 3D-Si increases with increasing dopant density and is higher than 100 meV at $N > 2 \times 10^{20}\ cm^{-3}$. As a result, the δE_G values of n^+ and p^- 2D-Si layers are about one-fourth and one-half of the δE_G values of doped 3D-Si, respectively. Thus, δE_G effects attenuate with increasing N of doped 2D-Si, namely, the effect of dopant ions on E_G is very small in 2D-Si layers, which is characteristic of 2D-Si. However, the physical mechanism of this δE_G reduction in 2D-Si is not yet understood at present. Consequently, the E_G difference between the heavily doped source and the nondoped 2D-Si channel is estimated to be very small, compared with that between the pn-junction in 3D-Si. We will discuss pn-junction structures in 2D-Si layer in Sect. 3.3, considering the BSM in the doped and intrinsic 2D-Si layers shown in Figs. 4 and 5.

3.2 Phonon confinement effects in doped 2D-Si

In analyzing the self-heating effects of ETSOIs, it is necessary to evaluate the phonon properties of doped 2D-Si. Thus, in this section, we discuss the impurity dopant effect on the PCEs in 2D-Si.

Figures 6(a) and 6(b) show the UV–Raman spectra of the n^+ and p^- 2D-Si layers, respectively. It is newly found that doped 2D-Si layers also show PCEs at $T_S < 1$ nm, such as asymmetrical broadening effects of Raman spectra, although the Raman spectra at $T_S > 2$ nm show typical Lorentzians. The asymmetrical broadening effects are the same as those of the intrinsic 2D-Si.[24] However, the Raman spectra of p^- 2D-Si layers show no Fano effects, which are usually observed in a heavily doped p^+-Si,[15] because the p^- dopant density in this study is less than $1 \times 10^{20}\ cm^{-2}$.

To compare the PCEs of the doped 2D-Si with those of 2D i-Si, we introduce two parameters, i.e., W_L and W_H, shown in the inset of Fig. 7(b), which are defined by full width at one tenth maximum (FWTM) of the Raman spectra in lower and higher-wave number regions from the first-

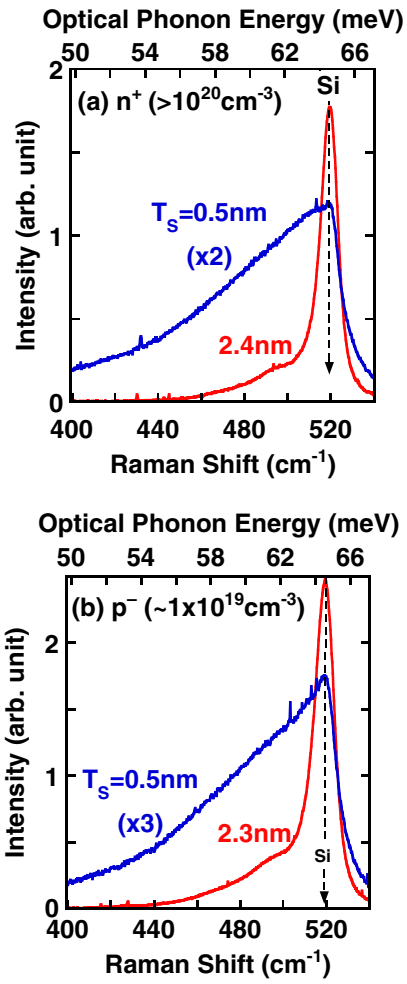

Fig. 6. (Color online) UV Raman spectra of (a) n^+ and (b) p^- layers at various T_S values. Upper and lower axes show the optical phonon energy E_P ($\equiv hc\omega$) and wave number ω, respectively, where c is the speed of light. Asymmetrical broadening of Raman spectra increases with decreasing T_S in both doped-Si layers.

order Raman scattering at the Γ point (520 cm^{-1}),[24] respectively. Here, the Si atom layer number N_L in 2D-Si is introduced using $N_L \equiv 4T_S/a + 1$, and N_L instead of T_S is found to be a better indicator for the evaluation of the Raman characteristics of 2D Si, because of the universal N_L dependences of W_L and W_H in various surface orientations of 2D-Si.[24] The N_L deviation δN_L is attributable to δT_S, resulting in $\delta N_L = 4/a \cdot \delta T_S \approx 1.5$ in this study.[24] Figure 7(a) shows that the W_L values of doped and nondoped 2D-Si layers are a function of N_L, and that the W_L values of doped and nondoped 2D-Si have an almost universal N_L dependence.[24] Therefore, the PCEs, that are related to the phonon properties of 2D-Si, are not affected by dopant atoms in n^+ 2D-Si, similarly to PCEs in heavily doped 1D-Si.[35] Moreover, Fig. 7(b) shows the N_L dependence of W_H, which is an indicator of the crystal quality of Si layers. Low W_H indicates good crystalline quality of doped 2D-Si even at $N_L < 10$. On the other hand, Fig. 7(c) shows the N_L dependence of the Raman peak downshift $\Delta\omega$ from 520 cm^{-1}, and almost all $\Delta\omega$ shows the universal N_L dependence. Consequently, the PCEs is independent of the dopant atom density, and thus the phonon properties of n^+ 2D-Si are considered to be the same as those of 2D i-Si.

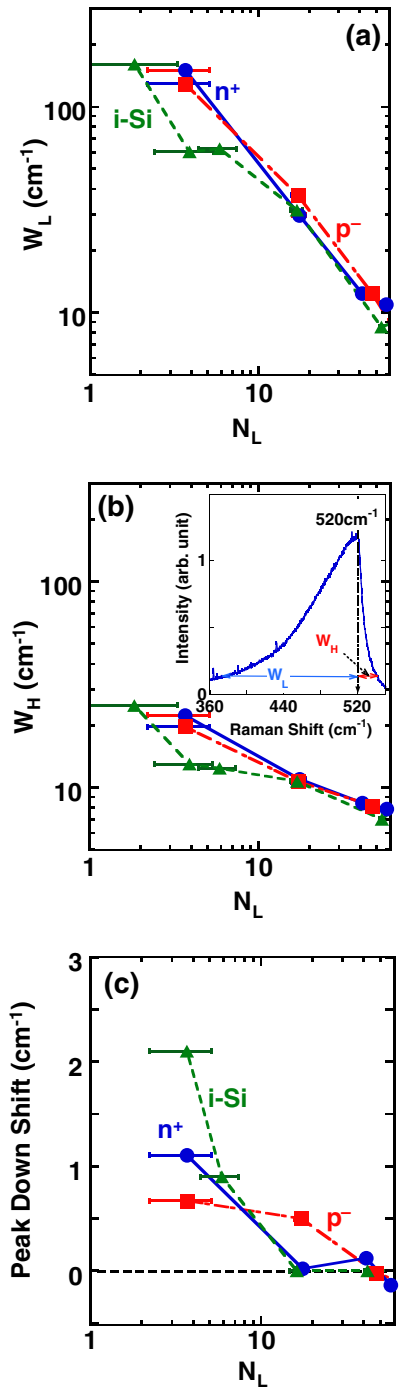

Fig. 7. (Color online) Si atom layer number N_L dependences of (a) W_L, (b) W_H, and (c) $\Delta\omega$ of n^+ (circles), p^- (squares), and i-Si (triangles) layers. Error bars of N_L are due to δT_S[24] and are about 1.5. The inset in (b) shows asymmetrical broadening parameters, i.e., W_L and W_H defined by the FWTM of the Raman peak value in the lower and higher wave number regions from 520 cm^{-1}, respectively. Almost all data have the same N_L dependence, and thus the PCEs are independent of dopant density.

3.3 Device design for pn-junction structures for future CMOS

Since E_G expands in the 2D-Si discussed in Sect. 3.1, it is necessary to reconstruct pn-junction structures for future ETSOIs to realize a high current drivability even at a low supply voltage V_{DD}, by reducing the built-in potential V_{BI} at the source pn junction and the threshold voltage V_{TH}. Moreover, the channel of ETSOIs should be the intrinsic Si

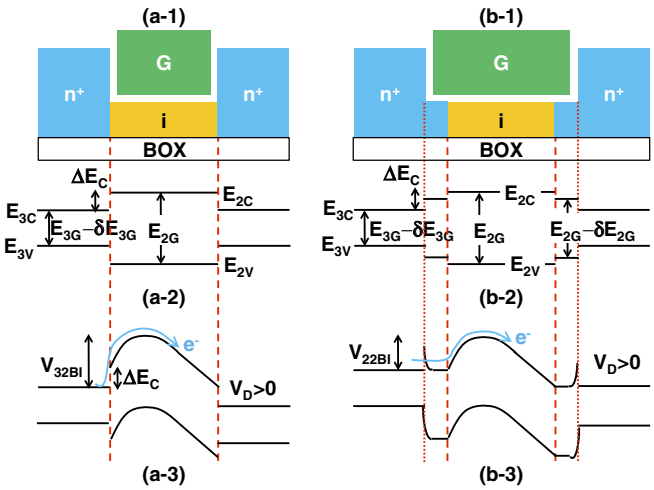

Fig. 8. (Color online) Schematic cross sections of n-ETSOI MOSFETs with (a-1) 3D-n$^+$-source/2D-i-channel heterojunction and (b-1) 2D-n$^+$-source/2D-i-channel homojunction structures. G denotes the gate electrode. (a-2)/(b-2) and (a-3)/(b-3) show the schematic bandgap and potential distributions at $V_D > 0$ from the source region to the drain region, respectively. In (b-2), E_{2C}, E_{2V}, E_{2G}, and δE_{2G} show the conduction band energy level, valence band energy level, bandgap, and bandgap narrowing of 2D-Si, respectively. E_{3C}, E_{3V}, E_{3G}, and δE_{3G} in (a-2) also show the conduction band energy level, valence band energy level, bandgap, and bandgap narrowing of 3D-Si, respectively. ΔE_C in (a-2) shows the conduction band offset between the 3D-Si and 2D-Si layers. V_{32BI} in (a-3) shows the abrupt build-in potential between source n$^+$ 3D-Si and i-channel 2D-Si. V_{22BI} in (b-3) shows the abrupt build-in potential between source n$^+$ 2D-Si and i-channel 2D-Si.

structure (i-Si), to avoid the V_{TH} fluctuation caused by the statistical fluctuation of impurity dopant atoms in the channel, as well as to suppress the Coulomb scattering of carriers.[36]

Three key points for future ETSOIs are the realization of 1) thinner channel Si layers composed of 2D-Si with a wide E_G (E_{2G}) to suppress the SCE, 2) i-channels to avoid V_{TH} fluctuation and suppress the Coulomb scattering of carriers, and 3) thick source/drain n$^+$ regions of 3D-Si with a narrow E_G (E_{3G}) to reduce the parasitic source/drain diffusion resistance. Therefore, Figs. 8(a) and 8(b) show two candidates for future ETSOIs with a 3D-n$^+$/2D-channel junction and a 2D-n$^+$/2D-channel junction (2D-junction structure), respectively. The pn junction edge of a 3D-n$^+$/2D-channel [Fig. 8(a-1)] exists just at the 3D-n$^+$/2D-channel heterojunction edge. On the other hand, a pn junction edge of the 2D-junction structure [Fig. 8(b-1)] exists inside the 2D-Si layers. In this study, we assume that the electron affinity of 2D-Si; χ_2, can be expressed by the following equation:

$$\chi_2 + \frac{E_{2G}}{2} = \chi_3 + \frac{E_{3G}}{2}, \tag{3}$$

where χ_3 is the electron affinity of 3D-Si.

In the case of the 3D-n$^+$/2D-channel structures shown in Fig. 8(a), according to the E_G expansion ΔE_G in the 2D-Si shown in Eq. (1) and the bandgap narrowing δE_{3G} of 3D doped Si shown in Eq. (2),[13] the conduction band offset ΔE_{32C} between the 3D-source and 2D-channel regions is assumed to be described by the following equation, according to the schematic band profile shown in Fig. 8(a-2):

$$\Delta E_{32C} = \frac{\Delta E_G + \delta E_{3G}}{2} = \frac{E_{2G} - E_{3G} + \delta E_{3G}}{2}. \tag{4}$$

On the other hand, the conduction band offset ΔE_{22C} between the 2D-source and 2D-channel regions can be given by the schematic band profile shown in Fig. 8(b-2):

$$\Delta E_{22C} = \frac{\delta E_{2G}}{2} \approx 0, \tag{5}$$

where δE_{2G} is the bandgap narrowing of doped 2D-Si and is negligible small (several tens of meV), as shown in Fig. 5.

Therefore, ΔE_{32C} in the 3D-n$^+$/2D-channel structure shown in Fig. 8(a) enhance V_{TH} as well as V_{BI}, because $V_{TH} \propto V_{FB} \propto \Delta E_{32C}$ (V_{FB} is the flat band voltage of the MOS gate), according to the potential distribution in Fig. 8(a-3). As a result, the V_{BI} of the 3D-n$^+$/2D-channel structure; V_{32BI}, can be obtained using Eq. (4), namely,

$$V_{32BI} \approx \Delta E_{32C} + \frac{E_{2G}}{2} = E_{2G} + \frac{\delta E_{3G} - E_{3G}}{2}. \tag{6}$$

On the other hand, the V_{BI} of the 2D-junction structure, V_{22BI}, can be expressed by considering the potential distribution in Fig. 8(b-3) and Eq. (5):

$$V_{22BI} \approx \frac{E_{2G}}{2} = V_{32BI} - \Delta E_{32C}. \tag{7}$$

Thus, V_{22BI} can be suppressed by ΔE_{32C}, compared with V_{32BI}. Therefore, the 3D-n$^+$/2D-channel structure shown in Fig. 8(a-1) is the worst case for reducing V_{BI}. However, V_{22BI} is higher than the V_{BI} of the conventional 3D-Si devices with narrow E_G.

As shown in Fig. 8(a-3), the conduction energy level of the channel, E_{2C}, is higher than that of the source, E_{3C}, which induces the energy spike due to ΔE_{32C} at the 3D-n$^+$/2D-channel heterojunction. As a result, the energy spike at the 3D-n$^+$/2D-channel heterojunction causes the electron velocity v_E reduction at the source pn-junction edge, which is the opposite effect of that in source heterojunction devices (SHOT) with high-electron velocity v_E injection from the source into the channel, using the excess kinetic energy between the high-E_C source and the low-E_C channel.[37,38] However, in the case of the pn junction edge inside 2D-Si, Fig. 8(b-3) shows that the energy spike does not affect v_E, since the pn depletion layer width of n$^+$ 2D-Si layers becomes very small, resulting in the tunneling effects of electrons at the source energy spike. Consequently, the 2D-junction structure shown in Fig. 8(b-1) is the optimum pn-junction for future ETSOIs.

Here, V_{BI} can be calculated as a function of the channel length L and T_S in both the 3D-n$^+$/2D-channel junction and 2D-junction structures for future ETSOIs, using $L = 3T_S$ scaling,[1] and Eqs. (1), (2), (6), and (7). Figure 9 shows the V_{BI} in 3D-n$^+$/2D-channel junction (dashed line) and 2D-junction structures (solid line) vs L and T_S. The V_{BI} of the 2D-Si channel continues increasing with decreasing T_S and is much higher than that of the 3D-Si pn-junction (arrow), because E_{2G} rapidly increases with decreasing T_S, as shown in Eq. (1). However, the V_{BI} of the 2D-junction structure can be reduced to be about 2/3 of that of the 3D-n$^+$/2D-channel structure. Consequently, in the case of $L \leq 10$ nm, to suppress the source energy spike at the pn junction in ETSOIs

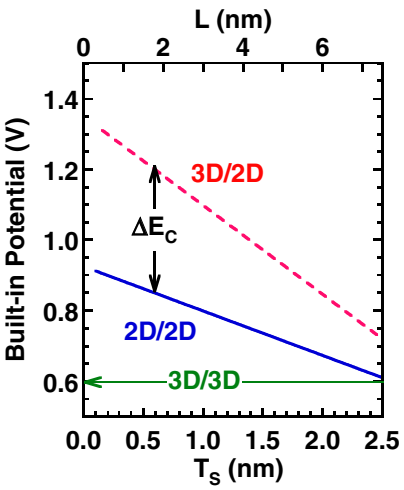

Fig. 9. (Color online) T_S and L (upper axis) dependences of calculated V_{BI} values of ETSOIs with 2D-junction (solid line) and 3D/2D pn-heterojunction (dashed line) structures which are determined using Eqs. (6) and (7), respectively, assuming $L = 3T_S$ scaling in ETSOIs.[1] The arrow shows the V_{BI} of the pn-junction in the 3D-Si.

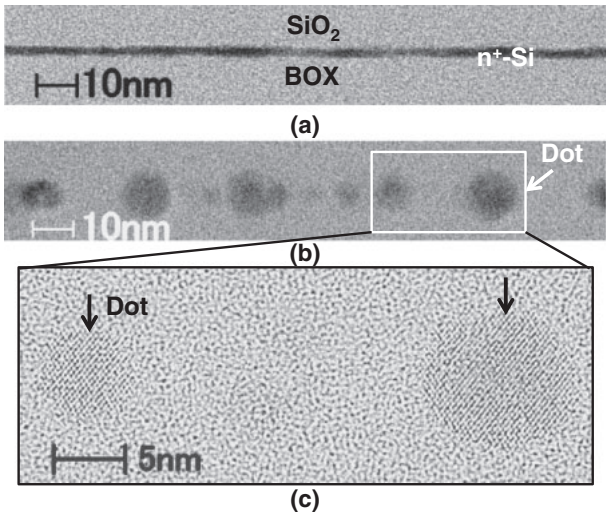

Fig. 10. TEM images of the cross section of (a) 1.5 nm n^+ 2D-Si sheet, (b) n^+ Si-dot regions, and (c) Si lattice images of Si dots, in the case of heavier doping at a phosphorus ion dose of $1 \times 10^{15}\,cm^{-2}$ into 55-nm-thick SOI, which is 25 times higher than that for n^+-Si in this work. (c) Si dots showing good lattice image.

composed of 2D-Si channels, it is crucial to reconstruct pn-junction structures for high-performance ETSOIs, such as the 2D-junction structure shown in Fig. 8(b).

3.4 Oxidation process limitation for forming heavily-doped 2D-Si

In the case of a relatively low dose ($4 \times 10^{13}\,cm^{-2}$) P^+-implanted n^+ 2D-Si, n^+ 2D-Si layer with $N_D \approx 4 \times 10^{20}\,cm^{-3}$ at $T_S \approx 0.5$ nm can be successfully formed, as discussed above. However, in the case of a much heavier P^+ ion implantation dose of $1 \times 10^{15}\,cm^{-2}$ which is 25 times as high as the above P^+ dose, the phosphorus atom density of n^+ 2D-Si is estimated to be much higher than $1 \times 10^{22}\,cm^{-3}$ at T_S less than about 2 nm.

Figure 10(a) shows a HRTEM observation of the cross section of 1.5-nm-thick n^+ 2D-Si layers, where the P^+ ion implantation dose is $1 \times 10^{15}\,cm^{-2}$. A uniform 2D-Si layer can be achieved. However, at $T_S < 1.5$ nm, Fig. 10(b) indicates that some area shows Si dot (0D-Si) formation, which is transformed from 1.5-nm-thick 2D-Si layers. In addition, Fig. 10(c) shows good Si lattice images of Si dots and the Si dot diameter is about 10 nm. The Si dot formation is the oxidation process limitation for fabricating 2D-Si layers, and is probably attributable to the very high phosphorus atom density of the 2D-Si layers, as will be discussed below.

Figure 11 shows the EDX results for the Si dots including the SiO_2 layers around the Si dots shown in Fig. 10(c), where the X-ray beam diameter is about 0.2 nm. According to the EDX peak counts of Si, O, and P, the atomic percentages of Si, O, and P are 35.8, 59.2, and 5.0%, respectively. Assuming that the EDX peak counts consist of Si dots with P and SiO_2, the Si atomic percentage in SiO_2 is equals to 29.6% which is exactly a half of the O atomic percentage (59.2%). As a result, Fig. 11 shows that the Si atomic percentage in the Si dots is estimated to be 6.2%, which is the total Si atomic percentage (35.8%) minus the Si atomic percentage in SiO_2 (29.6%), and thus the ratio of P atoms to Si atoms in the

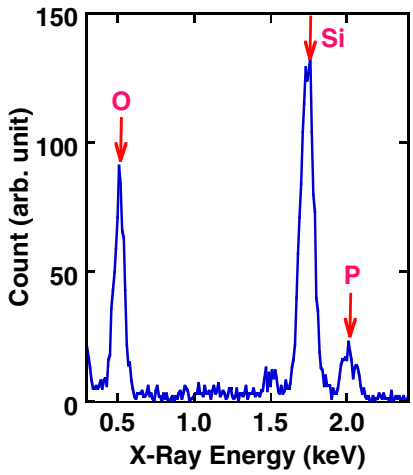

Fig. 11. (Color online) EDX result for n^+ Si dots including SiO_2 layers around Si dots, where X-ray diameter is about 0.2 nm. Atomic percentages of Si, O, and P are 35.8, 59.2, and 5.0%, respectively. As a result, the phosphorus concentration in the Si dots is estimated to be about $2 \times 10^{22}\,cm^{-3}$.

Si dots is 0.45, which equals 5%/(5% + 6.2%). Therefore, since the Si density is $5 \times 10^{22}\,cm^{-3}$,[13] the phosphorus density in the Si dots reaches about $2.2 \times 10^{22}\,cm^{-3}$, which is attributable to the phosphorous condensation effects of oxidizing the Si layers. This ultrahigh phosphorus density of the Si dots is about five times more than the simulation results of $4 \times 10^{21}\,cm^{-3}$ of the 1.5-nm-thick 2D-Si layer, and causes the melting point depression of the 2D-Si layers.

Consequently, this melting point depression of the 2D-Si layers possibly causes the Si dot formation, which is attributable to the recrystallization of melted 2D-Si on the BOX. This is the technical limitation of the oxidation method for fabricating doped 2D-Si layers. However, this Si dot formation is a potential new method of realizing Si dots, where it is possible to control the size and density of Si dots by optimizing the fabrication process.

4. Conclusions

We experimentally studied impurity dopant atom effects on BSM and PCEs in 2D-Si layers, and compared them with those in 2D i-Si.

The PL results showed that the emitted photon peak energy E_{PH} from n^+ 2D-Si layers also increases with decreasing 2D-Si thickness T_S. However, the E_{PH} of doped 2D-Si is slightly lower than that of 2D i-Si, which is attributable to bandgap narrowing effects. In addition, the bandgap narrowing of doped 2D-Si is much lower than that of the conventional doped 3D-Si. This bandgap narrowing reduction is a new finding for doped 2D-Si.

On the other hand, the PCEs of doped 2D-Si, evaluated by UV Raman spectroscopy, are almost independent of the impurity dopant density. Therefore, the phonon properties of doped 2D-Si layers are almost equal to those of undoped 2D-Si layers. As a result, it is not necessary to introduce a special design for the source/drain diffusion regions in ETSOIs, considering the above phonon properties.

In designing the device structure of future high-performance ETSOIs, three key points should be realized: 1) a thinner channel composed of 2D-Si with a wide E_G (E_{2G}) to suppress the SCE, 2) i-Si for suppressing both the V_{TH} fluctuation and the Coulomb scattering of carriers, and 3) thick source/drain diffusion regions of 3D-Si with a narrow E_G (E_{3G}) to reduce the parasitic source/drain resistances. Thus, we can introduce a new device design for an optimum pn-junction whose edge exists inside 2D-Si layers (2D-junction structure), to suppress the build-in potential barrier at the source pn-junction edge.

Moreover, we have clarified the oxidation process limitation for fabricating doped 2D-Si layers. In the case of heavily doped n^+ 2D-Si, phosphorous atoms condense and their density is higher than $1 \times 10^{22}\,cm^{-3}$ in the Si layer with less than 1.5 nm thickness, resulting in the melting point depression of Si. As a result, Si dots are formed by the recrystallization effects of the melted 2D-Si layers on the BOX. Thus, the Si dot formation is the process limitation for fabrication the 2D-Si layers.

Acknowledgements

We would like to thank Professor J. Nakata and Dr. Y. Hoshino of Kanagawa University for performing ion implantation. This work was partially supported by a Grant-in-Aid for Scientific Research from the Japan Society for the Promotion of Science (24560422).

1) A. Nazarov, J.-P. Colinge, F. Balestra, J.-P. Raskin, F. Gamiz, and V. S. Lysenko, *Semiconductor-on-Insulator Materials for Nanoelectronics Applications* (Springer, Berlin, 2011).
2) T. Irisawa, T. Numata, T. Tezuka, K. Usuda, N. Sugiyama, and S. Takagi, IEEE Trans. Electron Devices **55**, 649 (2008).
3) S. Saito, D. Hisamoto, H. Shimizu, H. Hamamura, R. Tsuchiya, Y. Matsui, T. Mine, T. Arai, N. Sugii, K. Torii, S. Kimura, and T. Onai, Jpn. J. Appl. Phys. **45**, L679 (2006).
4) S. Saito, N. Sakuma, Y. Suwa, H. Arimoto, D. Hisamoto, H. Uchiyama, J. Yamamoto, T. Sakamizu, T. Mine, S. Kimura, T. Sugawara, M. Aoki, and T. Onai, IEDM Tech. Dig., 2008, 19.5.
5) T. Mizuno, N. Sugiyama, T. Tezuka, Y. Moriyama, S. Nakaharai, and S. Takagi, IEEE Trans. Electron Devices **52**, 367 (2005).
6) T. Mizuno, N. Sugiyama, T. Tezuka, T. Numata, and S. Takagi, IEEE Trans. Electron Devices **50**, 988 (2003).
7) K. Uchida, H. Watanabe, A. Kinoshita, J. Koga, T. Numata, and S. Takagi, IEDM Tech. Dig., 2002, p. 47.
8) K. Uchida, J. Koga, and S. Takagi, J. Appl. Phys. **102**, 074510 (2007).
9) G. Tsutsui, M. Saitoh, and T. Hiramoto, IEEE Trans. Electron Devices **26**, 836 (2005).
10) B. K. Agrawal and S. Agrawal, Appl. Phys. Lett. **77**, 3039 (2000).
11) M. Tabe, M. Kumezawa, and Y. Ishikawa, Jpn. J. Appl. Phys. **40**, L131 (2001).
12) Z. H. Lu and D. Grozea, Appl. Phys. Lett. **80**, 255 (2002).
13) S. M. Sze and K. K. Ng, *Physics of Semiconductor Devices* (Wiley, New York, 2006).
14) K. Mizoguchi and S. Nakashima, J. Appl. Phys. **65**, 2583 (1989).
15) N. Fukata, T. Oshima, N. Okada, K. Murakami, T. Kizuka, T. Tsurui, and S. Ito, J. Appl. Phys. **100**, 024311 (2006).
16) K. W. Adu, H. R. Gutierrez, and P. C. Eklund, in *Nanosilicon*, ed. V. Kumar (Elsevier, Amsterdam, 2008) Chap. 7.
17) H. Richter, Z. P. Wang, and L. Ley, Solid State Commun. **39**, 625 (1981).
18) I. H. Campbell and P. M. Fauchet, Solid State Commun. **58**, 739 (1986).
19) L. Khriachtchev, M. Räsänen, S. Novikov, O. Kilpelä, and J. Sinkkonen, J. Appl. Phys. **86**, 5601 (1999).
20) G. Faraci, S. Gibilisco, P. Russo, and A. R. Pennisi, Phys. Rev. B **73**, 033307 (2006).
21) S. Piscanec, M. Cantoro, A. C. Ferrari, J. A. Zapien, Y. Lifshitz, S. T. Lee, S. Hofmann, and J. Robertson, Phys. Rev. B **68**, 241312(R) (2003).
22) L. Donetti, F. Gámiz, J. B. Roldán, and A. Godoy, J. Appl. Phys. **100**, 013701 (2006).
23) T. Mizuno, K. Tobe, Y. Maruyama, and T. Sameshima, Jpn. J. Appl. Phys. **51**, 02BC03 (2012).
24) T. Mizuno, T. Aoki, Y. Nagata, Y. Nakahara, and T. Sameshima, Jpn. J. Appl. Phys. **52**, 04CC13 (2013).
25) S. S. Iyer and Y.-H. Xie, Science **260**, 40 (1993).
26) A. G. Cullis, L. T. Canham, and P. D. J. Calcott, J. Appl. Phys. **82**, 909 (1997).
27) T. Sameshima, H. Watakabe, N. Andoh, and S. Higashi, Jpn. J. Appl. Phys. **45**, 2437 (2006).
28) Y. Takahashi, T. Furuta, Y. Ono, T. Ishiyama, and M. Tabe, Jpn. J. Appl. Phys. **34**, 950 (1995).
29) A. D. Lan, B. X. Liu, and X. D. Bai, J. Appl. Phys. **82**, 5144 (1997).
30) T. Mizuno, Y. Nakahara, Y. Nagata, Y. Suzuki, Y. Kubodera, Y. Shimizu, T. Aoki, and T. Sameshima, Ext. Abstr. Solid State Devices and Materials, 2013, p. 696.
31) Web [http://www.soitec.com/en/].
32) A. S. Grove, *Physics and Technology of Semiconductor Devices* (Wiley, New York, 1967).
33) Web [http://www.silvaco.com/].
34) L. Pavesi and R. Turan, *Silicon Nanocrystals* (Wiley-VCH, Weinheim, 2010).
35) S. C. Singh, H. B. Zeng, C. Guo, and W. P. Cai, *Nanomaterials* (Wiley-VCH, Weinheim, 2012).
36) T. Mizuno and A. Toriumi, Ext. Abstr. Int. Conf. Solid-State and Integrated Circuit Technology, 2010, p. 847.
37) T. Mizuno, Y. Moriyama, T. Tezuka, N. Sugiyama, and S. Takagi, Jpn. J. Appl. Phys. **50**, 010107 (2011).
38) T. Mizuno, M. Hasegawa, K. Ikeda, M. Nojiri, and T. Horikawa, Jpn. J. Appl. Phys. **50**, 04DC02 (2011).